INTERNATIONAL SOCIETY FOR SOIL MECHANICS AND GEOTECHNICAL ENGINEERING

IS-PORTO 2023
PROCEEDINGS

State-dependent dilatancy of sand based on hollow cylinder laboratory tests under shear strain cycles

Lukas Knittel[1#] and *Merita Tafili*[2]

[1]*Keller Grundbau GmbH, Renchen, Germany*
[2]*Ruhr-University of Bochum, Bochum, Germany*
[#]*lukas.knittel@keller.com*

ABSTRACT

The present study is devoted to the investigation of the dilatancy behaviour of a fine sand based on hollow cylinder tests. Medium and dense samples were tested at a constant average stress by applying torsional angles for shear strains $\gamma = 1$, 2, 3 and 4%. Dilatancy curves along with shear wave velocity measurements to investigate the influence of the shear strain amplitude γ^{ampl} in the shear modulus degradation curve are presented and discussed. The measured stress and strain paths were used to compare the performance of four advanced constitutive models especially in describing the dilatancy behaviour of sand. From the perspective of their constitutive equations, the differences between the simulations with various material models are examined. It may be concluded that all four models allow a proper prediction of torsional shear tests as long as a proper calibration of the material parameters is secured.

Keywords: torsional shear tests; constitutive models; stress-dilatancy; shear modulus degradation

1. Introduction

State variables defining the soil particles and their mechanical behaviour have the property to significantly fluctuate spatially. As a result, they don't present a continuous surface, which makes constitutive models and numerical simulations challenging to capture. Since temporal and spatial fractal courses cannot be traditionally distinguished, generic rates and gradients of σ'_{ij} and ε_{ij} are necessary for the calculation of processes in situ. In laboratory studies, σ'_{ij} and ε_{ij} are calculated as global quantities in order to conceive of soil descriptions. For the improvement of constitutive models, curve fitting is often used but without any physical justification.

According to Pradhan's research (Pradhan Tatsuoka and Sato 1989, Pradhan and Tatsuoka 1989), there is a relationship between τ/p and $d = -\dot{\varepsilon}_v/\dot{\gamma}$ that is independent of void ratio e and effective mean pressure p, despite fluctuations. (Rowe 1962, Roscoe 1970 and Bishop 1953) have already hypothesized that this behavior is energetic in nature. (Luong 1982) confirmed these findings and related them to the shear localization observed in the laboratory. The dissipation is maximized when σ'_{ij} and ε_{ij} adapt to one other. Coaxiality emerges as a result of this. Since, stress-dilatancy and coaxiality with global amounts still apply despite the fractality, crucial phenomena allow laboratory studies to be scaled up without having to examine each particle individually. In this context, numerous literature is devoted to the description of stress-dilatancy, e.g. (Bolton 1986, Chakraborty and Salgado 2010, De Silva et al. 2014, Frossard 1979, Guo and Su 2007, Houlsby 1991, Jacobsen 1989, Kabilamany and Ishihara 1990, Li, Dafalias and Wang 1999, Li 2002, Li and Dafalias 2000,

Schanz and Vermeer 1996, Shahnazari and Towhata 2002, Tatsuoka 1976, 1987, Tokue 1979, Vaid and Sasitharan 1992, Wan and Guo 1999, 2004).

The aim of this article is to obtain wild fluctuations of the relationship τ/p and d by considering hollow cylinder samples and still record the behavior of the soil by means of constitutive models. Only a few constitutive models effectively depict non-linear and inelastic behavior, as well as volume expansion due to dilatancy as a result of shear stress, even though many stress-dilatancy equations relating the ratio of strain increments to stress ratio have been proposed in the past. In simple elasto-plastic constitutive models, the dilatancy behavior is described with the so-called flow rule $\boldsymbol{m}$, i.e. with the direction of the plastic deformation rate. Due to the formulation, there is often no dilatancy below the critical state, hence only overcritical dilatancy is described (Li and Dafalias 2000, Been and Jefferies 1985). Also, the dilatancy is modeled for loading only (no increased contractancy upon loading reversals). For this reason, the simple elasto-plastic constitutive models can only roughly reproduce the dilatancy d. Multi-surface models (e.g. Sanisand model) claim to better predict due to a narrow flexible elastic range (kinematic hardening). The hypoplastic model with intergranular strain (IGS) describes this behavior via the formulation of the non-linear hypoplastic strain rate $Y\boldsymbol{m}\|\dot{\boldsymbol{\varepsilon}}\|$.

Various torsional cyclic shear tests in a hollow cylinder device will be undertaken in the scope of this effort, which will be guided by Pradhan's et al. (Pradhan Tatsuoka and Sato 1989a, Pradhan and Tatsuoka 1989) studies. These tests reveal the discontinuous change in both the dilatancy rate and its sign by the reversal of loading direction as well as the largest rate of colume contraction against the change in shear strain during unloading immediately after the reversal of loading

direction. The laboratory data are simulated with the Incremental Driver (Niemunis 2022) to validate different constitutive models. Therefore, four advanced material models for sand are used: the hypoplastic model according to von Wolffersdorf with the extension by the intergranular strain of Niemunis and Herle (Hypo+IGS) (Niemunis and Herle 1997), the model of (Dafalias and Manzari 2004), which incorporates a yield surface rendering an elastoplastic model formulation (Sanisand), the Intergranular Strain Anisotropy model of Fuentes and Triantafyllidis (ISA) (Fuentes and Triantafyllidis 2015), which introduces an extended intergranular strain and is based on formulations of hypoplasticity and elastoplasticity. As well as the hypoplastic model with historiotropic yield surface of (Grandas, Triantafyllidis and Knittel 2020) (Hypo+YS). The study reveals the influence of various flow rule definitions on the mechanical description of the state-dependent dilatancy during torsional cyclic loading. Moreover, on the case of Hypo+YS it is shown that a properly defined flow rule based on the generalization of Taylor's dilatancy rule (Taylor 1948) sensures the reproduction of the strong contractancy upon reversal loading not requiring additional state variables. Based on the measurement data, an analysis of the degradation of the shear modulus is carried out.

2. Symbols and Notation

In this article, vectors, and second-order tensors are represented with bold symbols, for example the effective Cauchy stress $\boldsymbol{\sigma}$ and stretching $\boldsymbol{\varepsilon}$. Continuum mechanics conventions are followed, i.e. compression is defined negative. $\|\boldsymbol{X}\| = \sqrt{tr\boldsymbol{X}^2}$ is the Frobenius norm of $\boldsymbol{X}$, tr $\boldsymbol{X}$ is the sum of the diagonal components of $\boldsymbol{X}$. The superscript $\sqcup^0$ marks a normalised tensor, i.e. $\boldsymbol{X}^0 = \boldsymbol{X}/\|\boldsymbol{X}\|$. Cauchy stresses are considered as effective ones. $\dot{\boldsymbol{\sigma}}$ is the co-rotational stress rate. The stretching tensor $\boldsymbol{\varepsilon}$ is the symmetric part of the velocity gradient.

The void ratio e is the ratio of the volume of the voids V_v to the volume of the solids V_s. $p = -1/3 \, tr \, \boldsymbol{\sigma}$ is the mean effective stress, $\varepsilon_v = tr \, \boldsymbol{\varepsilon}$ is the volumetric strain. For strain, ε_i is defined negative. When dealing with axisymmetric conditions, the Rendulic plane is commonly used. In a conventional triaxial compression or oedometric compression test the axial stress is denoted with σ_1' and the radial stress is denoted with σ_3'. The associated strains are ε_1 and $\varepsilon_2 = \varepsilon_3$. The Roscoe invariants for triaxial conditions are defined as $q = -(\sigma_1 - \sigma_2)$ and $\varepsilon_q = -2/3 \cdot (\varepsilon_1 - \varepsilon_2)$.

Initial values are labeled with the subscript $\sqcup_0$. The superscript $\sqcup^e$ or $\sqcup^p$ denotes the elastic or plastic portion of a quantity $\sqcup$, respectively. The elastic and plastic proportions of the shear strain γ are γ^e and γ^p. The shear modulus $G = \Delta\tau/\Delta\gamma$ is calculated as secant stiffness.

Any symmetric second order tensor can be written as vector with the principal values $\boldsymbol{X}_v = [X_1, X_2, X_3]$. Bold calligraphic letters denote fourth order tensors (e.g. $\boldsymbol{M}$). Tensor operations are written following the Einstein summation convention. In particular, the indices follow the lexicographic order: $\boldsymbol{X} \otimes \boldsymbol{Y} = X_{ij}Y_{kl}$, $\boldsymbol{X}:\boldsymbol{Y} = X_{ij}Y_{ij}$ and $\boldsymbol{L}:\boldsymbol{\varepsilon} = L_{ijkl}D_{kl}$. Second order unit tensor $\boldsymbol{I}$ is defined as $I_{ij} = \delta_{ij}$ and the fourth order tensor $\boldsymbol{I}$ as $I_{ijkl} = \delta_{ik}\delta_{jl}$, using the Kronecker delta symbol δ_{ij}.

3. Hollow cylinder device, testing material and sample preparation

The uniform "Karlsruhe fine sand" (mean grain size $d_{50} = 0.14$ mm, uniformity coefficient $C_u = d_{60}/d_{10} = 1.5$, minimum void ratio $e_{\min} = 0.677$, maximum void ratio $e_{\min} = 1.054$, grain density $\varrho_s = 2.65$ g/cm³, subangular grain shape) has been used in the experiments. The grain size distribution curve and a microscopic image of the grains is shown in Fig. 1. The preparation of the medium dense and dense sample by means of dry air pluviation out of a funnel in the hollow cylinder requires a special mould consisting of several separate mould plates (Fig. 2a-d). The inner membrane is slid over the base plate and secured inside with two O-rings first (Fig. 2a). Then the outer membrane is also slipped over the base plate and secured with two more O-rings (Fig. 2b). The multi-part mould may now be set up, the membrane attached using a vacuum, and the sample prepared in (Fig. 2c,d). After the preparation the sample could be adjusted in the device (Fig. 2e). In the hollow cylinder device it is possible to control independently the vertical force F, outer cell pressure p_a, inner cell pressure p_i and torsional moment M_T cyclically (Fig. 2f). This allows an independent oscillation of the three normal stresses (σ_z in vertical, σ_r in radial, $\sigma_{\theta z}$ in circumferential direction) and one shear stress component $\tau_{\theta z}$. In the experiments $p_a = p_i$ was chosen.
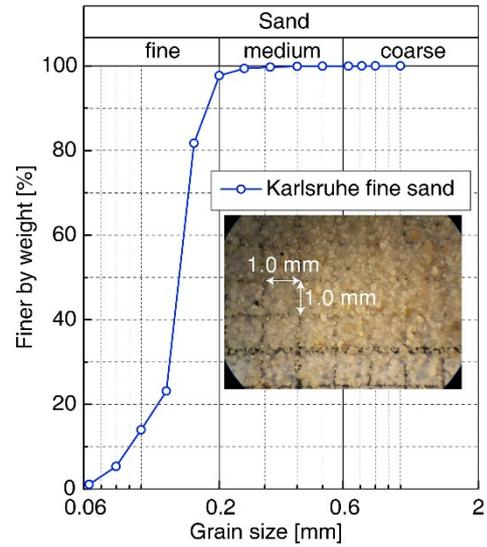
Figure 1. Grain size distribution curve of the used Karlsruhe fine sand and microscopic image of the grains.

The samples were tested with two different geometries under water-saturated conditions using a back pressure of 500 kPa. For a dense sample ($D_{r0} = 80\%$) with the large geometry ($h = 200$ mm, $d_a = 100$ mm and $d_a = 60$ mm) analogous to (Yamashita and Toki 1993, Tatsuoka et al. 1986, Georgiannou and Tsomokos 2008, Baziar and Sharafi 2011, Shahnazari and Towhata 2002, Yoshimine, Ishihara and Vargas 1998) and the small geometry ($h = 50$ mm, $d_a = 50$ mm and $d_a = 30$ mm) showed a similar material behavior. Here, similar curves

of the normalized shear stress τ/p [-] over the shear strain γ [%] were established. From this it can be concluded that the sample geometry has only a minor effect on the measurement results. Also no need for the correction of membrane penetration (Niemunis and Knittel 2020) could be found due to $d_{50} = 0.14$ mm.
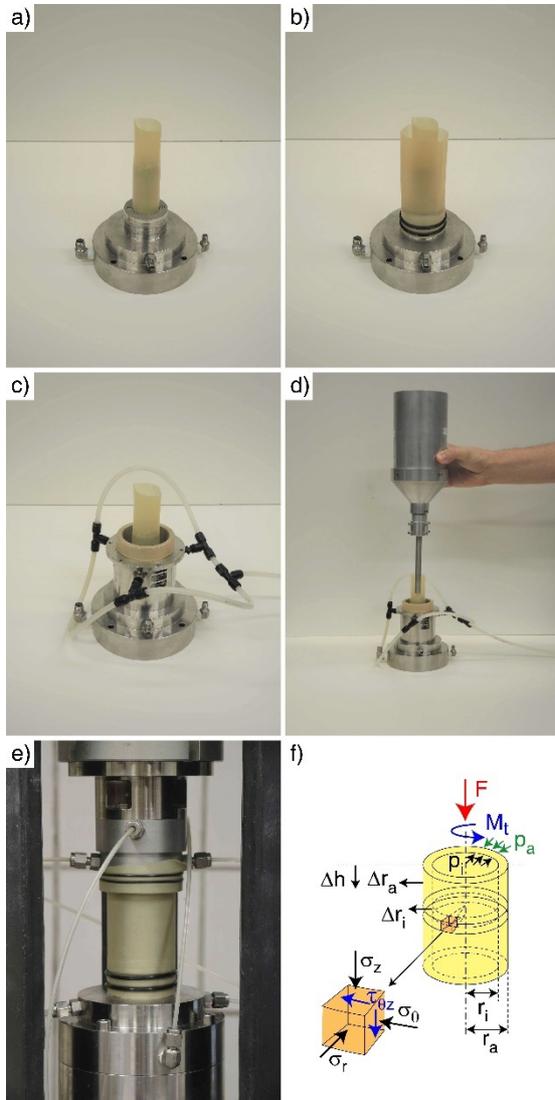
Figure 2. Preparation of the a) inner and b) outer membrane to the base plate. Conduction of the tubes for c) vacuum stabilization and d) preparation with air pluviation out of a funnel. e) hollow cylinder device and f) external loads and stresses acting on an element of soil in the experiment.

4. Test results and discussion

Only tests with the smaller geometry (h = 50 mm, d_a = 50 mm and d_a = 30 mm, Fig. 2e) are discussed below. Due to the mean grain diameter d_{50} = 0.14 mm, these small dimensions are permissible. Starting from an isotropic effective mean pressure p = 100 kPa, four drained load cycles were applied by controlling the torsion angle θ. Within one cycle, the torsion angle varied between $+\theta$ and $-\theta$. The amplitude of the torsion angle was increased from cycle to cycle. The torsion angles θ were chosen in such a way that shear strain amplitudes of γ = 1, 2, 3 and 4% were obtained. The individual load cycles were applied in a time period t = 3 min. The development of the shear stress τ with the

shear strain γ at constant mean pressure p was measured. Furthermore, in the last cycle of each test, several smaller unloading and reloading cycles with t = 1 min per cycle were applied to determine the elastic shear modulus G_e (Fig. 3 and 4).
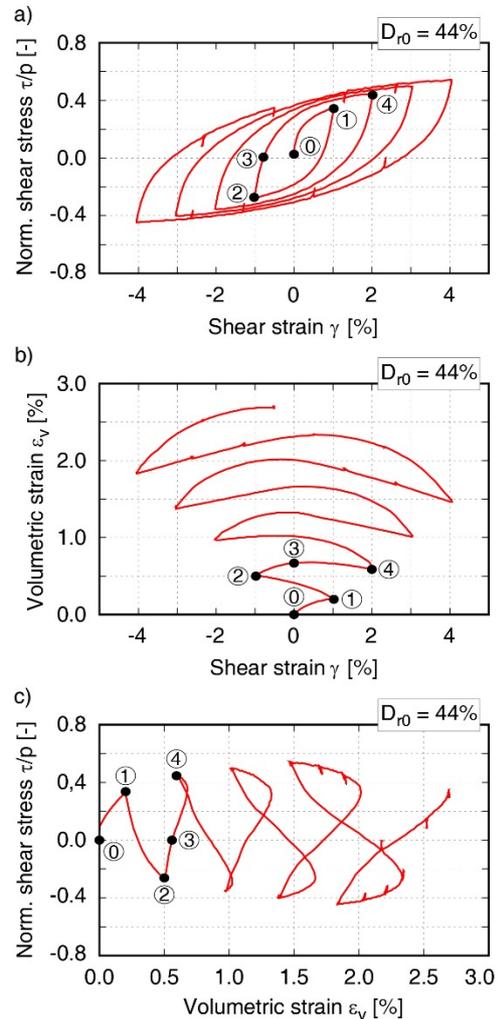
Figure 3. Test results with four shear cycles at a constant isotropic stress state p = 100 kPa. a) normalized shear stress τ/p as a function of shear strain γ and b) volumetric strain ε_v over shear strain γ and c) normalized shear stress τ/p over the volumetric strain ε_v for a sample with D_{r0} = 44%.

The Figs. 3a and 4a show the development of the normalized shear stress τ/p with the specified shear strain γ during the cyclic loading with the small unloading and reloading steps in the last cycle for a medium (D_{r0} = 44%) and dense D_{r0} = 72%) sample. The normalized shear stress τ/p changes discontinuously in both load directions. Immediately after the start of the load (i.e. just above point 0), an almost linear behavior is evident, after which the curve flattens non-linearly (point 0 → point 1). After each reversal of the load direction, the well-known increase in rigidity can be observed. With increasing shear strain in the new direction, the stiffness then decreases again. A comparison of the hysteresis loops for the medium (D_{r0} = 44%) and dense D_{r0} = 72%) sample illustrates the increase in stiffness with increasing relative density, which is reflected in larger stress ratios τ/p reflects γ at the same shear strain.

The curves of the volumetric strain ε_v over the shear strain γ obtained from the tests are shown in the Fig. 3b and 4b. A positive increment (increase) of the volumetric strain ε_v corresponds to contractive behavior (see point 0 → point 1), a negative increment (decrease) to dilative behavior (see point 3 → point 4). It turns out that the dilatant behavior of the dense sample is more pronounced than that of the medium dense sample (cf. point 3 → point 4). This is reflected in the more strongly curved sections of the curves, in which the volumetric expansion decreases and, accordingly, an increase in volume takes place.
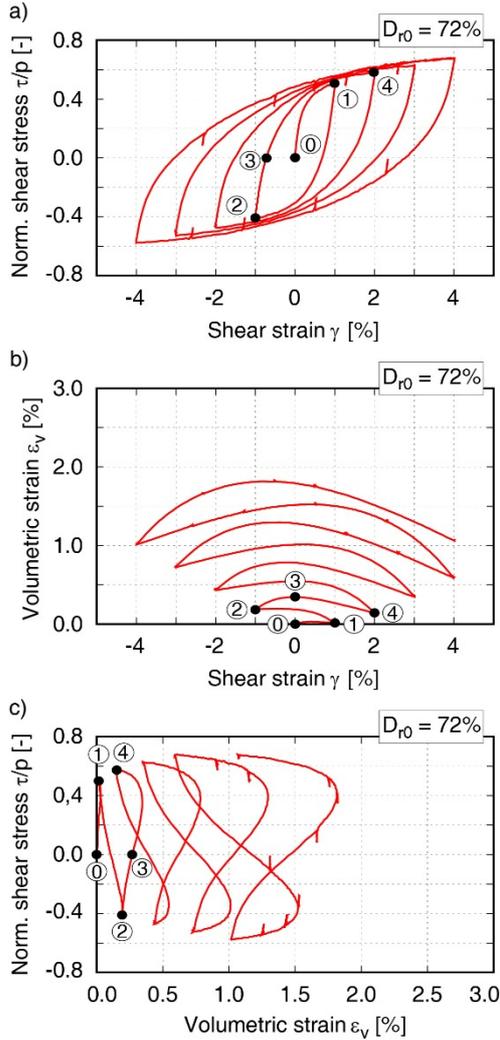
Figure 4. Test results with four shear cycles at a constant isotropic stress state p = 100 kPa. a) normalized shear stress τ/p as a function of shear strain γ and b) volumetric strain ε_v over shear strain γ and c) normalized shear stress τ/p over the volumetric strain ε_v for a sample with D_{r0} = 72%.

In Fig. 3c, the medium dense sample shows an accumulated volumetric strain of $\varepsilon_v \approx 3\%$ after completing the four cycles, while the corresponding value of the dense sample is only in the range 1 % $\leq \varepsilon_v \leq$ 2% lies. The dilatant behavior becomes more noticeable as the shear strain increases. In addition, there is the dependence on the shearing direction. For example, if the sample first behaves contractive and then dilative within one cycle, contractive behavior is observed immediately after the reversal of the shear direction. A further

variation of the dilatant behavior may be seen in Fig. 3c and 4c. When the normalized shear stress τ/p moves into the -0.2 % $\leq \tau/p \leq$ 0.4 range, only a positive volumetric strain ε_v is visible. As the normal shear stress τ/p rises, a dilative behavior emerges in this area.

Fig. 5 shows the relationship between the normalized shear stress τ/p and the dilatancy $d = -\dot{\varepsilon}_v/\dot{\gamma}_p$ for the medium and dense sample. The evaluation of the strain rates used for the calculation of the dilatancy was done with the total strains, i.e. without subtracting the elastic shear strain γ^e, which was originally supposed to be derived by (Pradhan and Tatsuoka 1989) from the small unloading and reloading cycles. A representation analogous to the relationship created by (Pradhan and Tatsuoka 1989) requires the exclusive use of the plastic part of the shear strain γ^p. Unfortunately, the measurement data from the small unloading and reloading cycles proved to be too imprecise to determine the elastic shear strain γ^e and thus the plastic shear strain $\gamma^p = \gamma - \gamma^e$. Nevertheless, using the data in Fig. 5, the friction angle $\varphi_{PTL} = \arctan(\tau/p)$ on the phase transformation line (PTL) can be calculated from the stress ratio τ/p at $-\dot{\varepsilon}_v/\dot{\gamma}_p = 0$. This results in $\varphi_{PTL} \approx$ 24° for the medium and the dense sample.
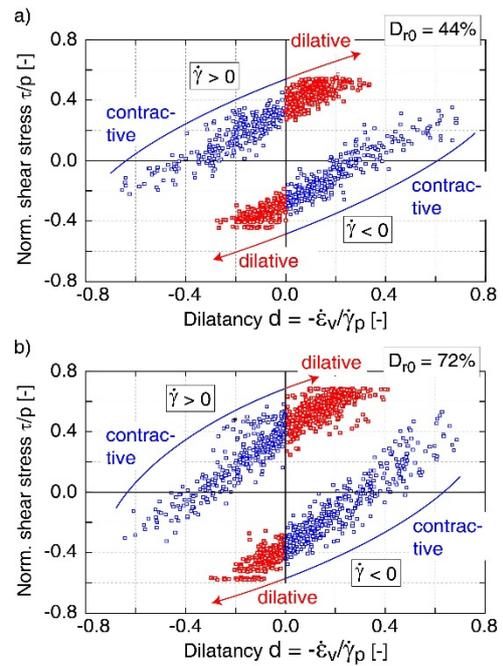
Figure 5. Normalized shear stress τ/p [-] as a function of the dilatancy d [-] for samples with a) D_{r0} = 44% and b) D_{r0} = 72%. Evaluation of the dilatancy with the total strains without subtracting the elastic part.

5. Determination of shear modulus degradation

In addition to the hollow cylinder triaxial tests with loading and unloading steps, measurements of the shear wave velocity with piezoelectric elements (bender elements) were carried out in a triaxial testing device according to (Knittel 2020). The purpose was to figure out how the shear modulus G degraded across the shear strain amplitude γ^{ampl} in both test series. The maximum value of the secant stiffness G_{max} was calculated from the

shear wave velocity v_s. The in- and output signals of the Bender Element measurements on a sample with a relative density $D_{r0} = 44\%$ at an average pressure $p = 100$ kPa are shown in Fig. 6 as electrical in- or output voltage $U_{\sqcup}$ over time t.
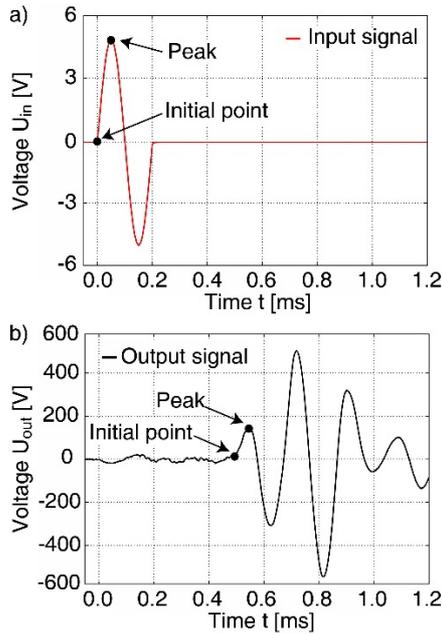
Figure 6. Bender Element measurements in a triaxial testing device on a medium dense sample ($D_{r0} = 44\%$) at effective mean pressure $p = 100$ kPa: a) in- and b) output signal.

The duration time may be calculated using a Matlab script and the peak-to-peak technique, or by taking into account the first usage as a time differential between the input and output signals. Both approaches took the same amount of time to complete. The shear wave velocity v_s may be estimated using the duration time and sample height h, from which the travel route can be deduced after subtracting twice the bender elements penetration length into the sample. From $G_{max} = v_s^2 \cdot \rho$ the maximum shear modulus for the dense sample ($D_{r0} = 72\%$) results in $G_{max} = 61.41$ MPa and for the medium dense sample ($D_{r0} = 44\%$) in $G_{max} = 46.83$ MPa.

Small unloading and reloading cycles were performed in the last cycle of the hollow cylinder triaxial tests to estimate the elastic range for the course of the deterioration of the shear modulus G across the shear strain amplitude G. The hysteresis loop with the unloading and reloading cycles for the dense sample is shown in Fig. 3b, from which the secant stiffness was calculated. The degradation of the shear modulus can be determined with the secant stiffnesses obtained from Fig. 3 for the dense sample and the values determined analogously for the medium dense sample as well as the Bender Element measurements.

Fig. 7a shows the determined curves of the shear modulus G of the two samples over the shear strain γ. As expected, the dense sample has a larger maximum shear modulus G_{max} than the medium dense. Both curves flatten out with increasing shear strain amplitude γ^{ampl} in accordance with the principle of the back-bone curve. Normalizing the shear modulus G with the maximum value G_{max} in Fig. 7b shows the characteristic course of

the degradation of the shear modulus, which is almost independent of the relative density D_{r0}.
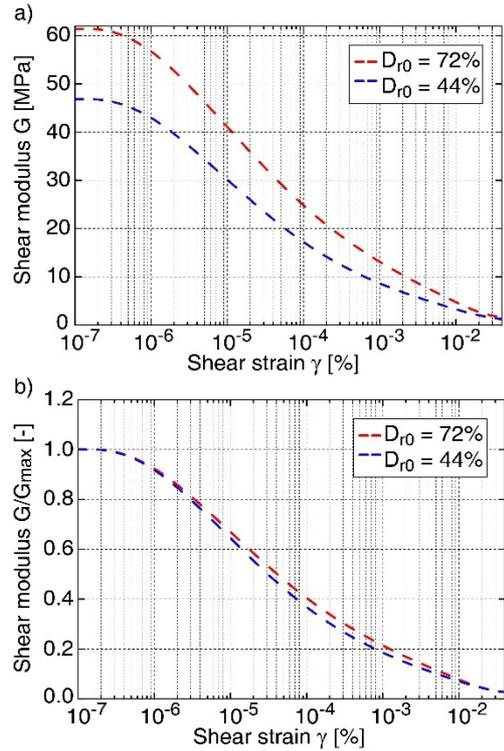
Figure 7. a) Degradation of the shear modulus G with the shear strain γ for samples with a relative density $D_{r0} = 44\%$ (blue) and $D_{r0} = 72\%$ (red) and b) normalized curves of G regarding G_{max}.

6. Mechanical modelling of torsional cyclic shear tests with four advanced constitutive models

Four advanced constitutive models are used for the simulations of the aforepresented experiments in the following. The considered models consist of the hypoplastic model (Wolffersdorff 1996) with intergranular strain (Niemunis and Herle 1997) (Hypo+IGS), the intergranular strain anisotropy model (Fuentes 2015), the simple anisotropic sand model (Sanisand) version of 2004 (Dafalias and Manzari 2004) and the newly proposed hypoplastic model with historiotropic surface (Hypo+YS) (Grandas, Triantafyllidis and Knittel 2020). In the next Secs. 6.1-6.4 the constitutive equations governing the models formulations are briefly summarized. Afterwards, in Sec. 6.5 the simulations are discussed.

6.1. Hypoplasticity with Intergranular Strain (Hypo+IGS)

The hypoplastic model for sand proposed in 1996 (Wolffersdorff 1996) is herein used in conjunction with the intergranular strain porposed in 1997 (Niemunis and Herle 1997). The new state variable $\boldsymbol{h}$ named intergranular strain has been introduced for hypoplastic models in order to improve their performance in the range of small load cycles.

In general, the constitutive equation of Hypo+IGS relates the objective effective stress rate $\dot{\boldsymbol{\sigma}}$ with the strain rate $\dot{\boldsymbol{\varepsilon}}$:

$$\dot{\boldsymbol{\sigma}} = \boldsymbol{M}(\boldsymbol{\sigma}, \vec{\dot{\boldsymbol{\varepsilon}}}, \boldsymbol{h}, e): \dot{\boldsymbol{\varepsilon}} \qquad (1)$$

wherein $\boldsymbol{M}$ is a fourth order tensor representing the tangential stiffness. It is calculated from the barotropic and pyknotropic hypoplastic tensors $\boldsymbol{L}(\boldsymbol{\sigma}, e)$ and $\mathrm{N}(\boldsymbol{\sigma}, e)$ which are suitably increased, depending on the loading direction and the size of the evolved intergranular strain. For example, for monotonic deformation with $\dot{\boldsymbol{\varepsilon}} \propto \vec{\boldsymbol{h}}$ the hypoplastic equation:

$$\dot{\boldsymbol{\sigma}} = \left(\boldsymbol{L} + \mathrm{N}\frac{\dot{\boldsymbol{\varepsilon}}}{\|\dot{\boldsymbol{\varepsilon}}\|} \right): \dot{\boldsymbol{\varepsilon}} \qquad (2)$$

is recovered. For reversed deformation, i.e. $\dot{\boldsymbol{\varepsilon}} \propto \vec{\boldsymbol{h}}$ (Niemunis 2003) the stiffness is increased by the material parameter m_R and the nonlinear part of the hypoplastic equation is deactivated, hence $\boldsymbol{M} = m_R \boldsymbol{L}$. Finally, under neutral strain rate, i.e. $\dot{\boldsymbol{\varepsilon}} \perp \vec{\boldsymbol{h}}$ a slightly increased stiffness is obtained using the parameter $m_R \leq m_T \geq 1$, i.e. $\boldsymbol{M} = m_T \boldsymbol{L}$.

For further details on the equations of Hypo+IGS, the attention of the reader is drawn to (Wolffersdorff 1996, Niemunis and Herle 1997, Niemunis 2003).

6.2. Intergranular Strain Anisotropy model (ISA)

The intergranular strain anisotropy (ISA) model is proposed in (Funetes 2014) by extending and reformulating the intergranular strain of (Niemunis and Herle 1997). The elasto-plastic formulation of the intergranular strain coupled with a plastic mechanical response of the model under fully mobilized intergranular strain renders the model elasto-hypoplastic. This is achieved through a yield and a bounding surface within the intergranular strain space:

$$\begin{aligned} F_H &= \|\boldsymbol{h} - \boldsymbol{c}\| - R/2 \quad \text{(yield surface)}, \\ F_{Hb} &= \|\boldsymbol{h}\| - R \qquad \text{(bounding surface)}, \end{aligned} \qquad (3)$$

wherein the second order tensors $\boldsymbol{h}$ and $\boldsymbol{c}$ denote the intergranular strain and the back intergranular strain, respectively. The size of the yield surface is governed by its radius, the material parameter R at which only slight degradation of the shear modulus is allowed, i.e. the ratio $G/G_{\max} \approx$ const. in Fig. 7.

The constitutive equation for the mechanical behavior interrelates the stress rate $\dot{\boldsymbol{\sigma}}$ with the strain rate $\dot{\boldsymbol{\varepsilon}}$ via the hypoplastic tangential stiffness $\boldsymbol{E}$:

$$\dot{\boldsymbol{\sigma}} = \boldsymbol{E}: (\dot{\boldsymbol{\varepsilon}} - \dot{\boldsymbol{\varepsilon}}^p) \qquad (4)$$

with the plastic strain rate dependent on $\dot{\boldsymbol{\varepsilon}}^p(\boldsymbol{\sigma}, \dot{\boldsymbol{\varepsilon}}, \boldsymbol{h}, e)$. Inside the intergranular yield surface $\|\boldsymbol{h}\| < R$ the response of the model is (hypo)elastic, i.e. $\dot{\boldsymbol{\varepsilon}}^p = 0$ in Eq. (4). During the kinematic hardening of the yield surface towards the bounding surface the so-called transition regime takes place, hence slight plastic strain rates are allowed. Once the intergranular strain lies on the bounding surface, any influence of it is erased and the

model is in fully mobilized state turning hypoplastic. In the original publication (Fuentes 2014) it is claimed that a smooth transition between elastic and hypoplastic regime is achieved. This might hold for triaxial tests as shown in various works for sands (Fuentes and Triantafyllidis 2015, Machacek et al. 2021, Poblete, Fuentes and Triantafyllidis 2016, Wichtmann, Fuentes and Triantafyllidis 2019) and clays (Duque et al. 2021, Fuentes, Tafili and Triantafyllidis 2018, Tafili et al. 2022, Tafili and Triantafyllidis 2020), but not necessarily also for cyclic torsional tests as will be shown in Sec. 6.5.

6.3. Simple anisotropic sand model (Sanisand)

The Sanisand family of models has attracted increased attention from researchers in the last decades resulting in a significant number of published models, for e.g. (Dafalias and Manzari 2004, Taiebat and Dafalias 2007, Lashkari 2010, Liu and Pisanò 2019, Liu et al. 2019). Lastly, the yield surface of this model was reduced even to zero and becomes identical to the stress point itself, and plastic loading occurs for any direction of the stress ratio rate on which the loading and plastic strain rate directions now depend, rendering the model incrementally non-linear (Dafalias and Taiebat 2016). Hence the model is in this version transformed to a kind of hypoplasticity. Still, the most used version is the one developed by (Dafalias and Manzari 2004) and therefore will be used in the following.

It represents a "wedge"-type yield surface in p-q space in generalized form obeying the following relationship:

$$f = [(\boldsymbol{s} - p\boldsymbol{\alpha}): (\boldsymbol{s} - p\boldsymbol{\alpha})]^{1/2} - \sqrt{2/3}pm = 0 \qquad (5)$$

with the deviatoric stress tensor $\boldsymbol{s}$, back stress ratio tensor $\boldsymbol{\alpha}$ and the material parameter m defining the opening of the wedge. Besides these variables, a fabric-dilatancy internal tensorial variable $\boldsymbol{z}$ to model the effect of fabric change on dilatancy is introduced into the model. The elasto-plastic (subscript ep) evolution equation of the stress then takes the following dependencies:

$$\dot{\boldsymbol{\sigma}} = \boldsymbol{E}^{ep}(\boldsymbol{\sigma}, \boldsymbol{\alpha}, \boldsymbol{z}, e, \dot{\boldsymbol{\varepsilon}}): \dot{\boldsymbol{\varepsilon}} \qquad (6)$$

with the elastoplastic tangent stiffness tensor $\boldsymbol{E}^{\mathrm{ep}}$. For further details on the mathematical formulation of Sanisand, the interested reader is referred to (Dafalias and Manzari 2004).

6.4. Hypoplasticity with Historiotropic Surface (Hypo+YS)

The model with historiotropic yield surface developed by (Grandas, Triantafyllidis and Knittel 2020) combines the hypoplastic equation with a yield surface in the stress space (Knittel 2020). The yield surface is used to describe the intensity of anelastic flow by defining the state of the soils by means of the current stress, void ratio and back-stress tensor $\boldsymbol{\sigma}_B$. Nevertheless, the response of the material model within the flow surface is not elastic, instead the intensity of plastic strain rates becomes dependent on the distance to the flow surface.

The main evolution equation of the model interrelates the stress rate with the strain rate using a hypoplastic-type of formulation:

$$\dot{\boldsymbol{\sigma}} = \boldsymbol{E} : (\dot{\boldsymbol{\varepsilon}} - Y\mathbf{m}\|\dot{\boldsymbol{\varepsilon}}\|) \qquad (7)$$

wherein the fourth rank tensor $\boldsymbol{E}(\boldsymbol{\sigma}, e)$ is a hyperelastic stiffness, $Y(\boldsymbol{\sigma}, e, \boldsymbol{\sigma_B})$ is the so-called degree of nonlinearity and $\boldsymbol{m}(\boldsymbol{\sigma}, e, \boldsymbol{\sigma_B}, \vec{\boldsymbol{\varepsilon}}^*)$ is the flow rule. $\boldsymbol{\varepsilon}^*$ denotes the deviatoric part of the strain tensor.

As a distinctive feature of the model, a generalization of Taylor's dilatancy rule (Taylor 1948) ensures to reproduce the strong contractancy upon reversal loading observed in experiments without the introduction of additional state variables as for instance the fabric-dilatancy tensor. For detailed insight into the model formulation, the reader's attention is drawn to (Knittel 2020).

6.5. Simulations

The presented material models are now examined in more detail using the experimental results of the torsional shear tests. For each material model, a user defined material routine (UMAT) by A. Niemunis (hypoplasticity with intergranular strain), M. Tafili (Sanisand model and ISA model) and C. Grandas (Hypo+YS) was available. The Elementtest simulations were performed with the software *incremental driver* developed by (Niemunis 2022). All material routines are implemented with the programming language FORTRAN, as material subroutines from the commercial finite element software Abaqus standard. The classic "elastic predictor" scheme (Simo and Hughes 1998) has been followed to perform the numerical implementation of Sanisand and ISA. A substepping scheme with small strain increments has been implemented to guarantee numerical convergence.

The torsional cyclic shear tests were carried out with a constant effective mean pressure of $p' = 100$ kPa. This stress condition was achieved by isotropic consolidation. Therefore, the initial condition $\sigma_1' = \sigma_2' = \sigma_3' = 100$ kPa is used in the simulations. Furthermore, the initial void ratio e as well as the initial values of internal variables like the intergranular strain (Hypo+IGS and ISA) or the back stress tensor (Sanisand and Hypo+YS) are needed. The initial void ratio is calculated following the relation:

$$e_0 = e_{\max} - D_{r0}(e_{\max} - e_{\min}) \qquad (8)$$

which for the medium dense sample renders $e_0 = 0.888$ and for the dense sample $e_0 = 0.783$. Here, an initially fully-mobilized intergranular strain in isotropic direction i.e. $\boldsymbol{h} = -R/\sqrt{3} \cdot \mathbf{1}$ (Hypo+IGS and ISA) was assumed. The intergranular back stress tensor was then assumed as half the intergranular strain i.e. $\boldsymbol{c} = -R/(2\sqrt{3}) \cdot \mathbf{1}$ (ISA) and the back stress tensor equal to the initial stress state $\boldsymbol{\sigma_B} = \boldsymbol{\sigma_0}$ (Sanisand and Hypo+YS). Each loading step was performed using proportional paths with 1000 increments and cartesian controls with $\Delta p' = 0$ kPa and $\Delta\gamma_{13}$ corresponding to the shear strain amplitudes

specified in Sec. 4. Other shear strains were held constant $\Delta\gamma_{12} = \Delta\gamma_{23} = 0$.

Even though the material parameters of all models have been calibrated on the extensive Karlsruhe fine sand database in (Wichtmann, Fuentes and Triantafyllidis 2019) it was not able to reproduce a good agreement between simulations and new torsional experiments. Therefore, a recalibration of the models have been performed resulting to the parameters in Tables 1 - 3.

The hypoplastic model with intergranular strain requires the calibration of 8 parameters for monotonic loading and additional 5 parameters for the intergranular strain, hence for cyclic loading, as listed in Table 1. Hereby, the parameters calibrated in (Wichtmann, Fuentes and Triantafyllidis 2019) using monotonic and cyclic triaxial tests were used as a fitting basis. The parameter defining the granulat hardness h_s as well as the parameters responsible for the dilatancy α and β and two of the IGS parameters β_R and χ have been varied in order to obtain good reproduction of both torsional cyclic shear tests with different densities.

Table 1. Material parameters of Hypo+IGS for Karlsruhe fine sand

φ_c [-]	e_{i0} [-]	e_{c0} [-]	e_{d0} [-]	h_s [MPa]	n [-]
33.1°	1.212	1.054	0.677	3000	0.27
α [-]	β [-]	R [-]	m_R [-]	m_T [MPa]	β_R [-]	χ [-]
0.11	2.0	0.0001	2.2	1.1	0.2	2.8

The ISA model requires the calibration of 12 parameters involved in the description of the mechanical behaviour of sands under monotonic loading and additionally 6 parameters defining the intergranular strain anisotropy. Again, the parameters calibrated in (Wichtmann, Fuentes and Triantafyllidis 2019) were used for the first run-up and then adjusted for better agreement with the cyclic torsional shear experiments. The final parameter set used for both experiments in this study is presented in Table 2.

Table 2. Material parameters of ISA for Karlsruhe fine sand

e_{i0} [-]	λ_i [-]	n_{pi} [-]	n_e [-]	ν [-]	e_{c0} [-]
1.21	0.0057	0.7	1.01	0.3	1.067
λ_c [-]	n_{pc} [-]	M_c [-]	c [-]	n_d [-]	f_{b0} [-]
0.00573	0.68	1.2	0.7	5.0	2.0
R [-]	m_R [-]	β [-]	χ_h [-]	c_z [-]	r_F [-]
0.00014	6.5	1.0	7.0	5000	1.5

The determination of in total 15 material parameters, as listed in Table 3, is required for the Sanisand model. Therefore, undrained monotonic and cyclic triaxial tests, oedometric tests as well as drained monotonic tests are necessary. These parameters were also taken from (Wichtmann, Fuentes and Triantafyllidis 2019) and were adapted here for the relevant experiments. The final parameter set is summarized in Table 3.

Table 3. Material parameters of Sanisand for Karlsruhe fine sand

e_0	λ	ξ	M_c	M_e
[-]	[-]	[-]	[-]	[-]
1.103	0.0057	0.205	1.35	0.945
m	G_0	ν	h_0	c_h
[-]	[-]	[-]	[-]	[-]
0.08	120	0.25	4.0	0.95
n_b	A_0	n_d	z_{max}	c_z
[-]	[-]	[-]	[-]	[-]
0.0001	0.9	1.5	3.0	100

The recently developed constitutive model with a historiotropic yield surface (Grandas, Triantafyllidis and Knittel 2020) requires the calibration of in total 16 parameters consisting of 3 parameters for the hyperelastic stiffness tensor, 4 for the critical state, 3 for the limiting compression curve, two for the dilatancy and 4 parameters for the yield surface involving oedometric tests as well as monotonic and cyclic triaxial tests for their calibration. The first draft of the parameters was taken from (Grandas, Triantafyllidis and Knittel 2020) and then adjusted for the simulations to be shown in sequel. The adjusted parameters of Hypo+YS used for both simulations are listed in Tab. 4.

Table 4. Material parameters of Hypo+YS for Karlsruhe fine sand

α	n	c	φ_c
[-]	[-]	[-]	[-]
0.1	0.677	0.001096	33.1°
e_{c0}	n_{Bc}	h_{sc}	c_2
[-]	[-]	[MPa]	[-]
1.054	0.27	4000	50
n_{Peak}	n_{YD}	e_{i0}	c_b
[-]	[-]	[-]	[-]
2	1	1.1	0.6
n_{PTL}	n_0	n_{Bi}	h_{si}
[-]	[-]	[-]	[MPa]
2	1.2	0.48	8400

Figs. 8 and 9 show the numerical calculations in blue for the two experiments in red with all models side by side for better comparison. For the simulations, the parameters were varied until the same parameter set was used to best represent the results of both the medium dense ($D_{r0} = 44\%$) and the dense sample $D_{r0} = 72\%$). The parameter sets used for the calculations with the models, with which the results in Figs. 8 and 9 were obtained are summarized in Tables 1 - 4. Of course, better agreement with the simulations could be obtained with two different sets of parameters.

The numerical calculations show that cyclic loading tends to be captured well with Hypo+IGS. However, both the dilatancy and the shear stress are significantly overestimated via the nonlinear function of the model for both tests. Hence, the accumulation of volumetric strain ε_v, which plays a crucial role in deformation predictions under cyclic loading, is overestimated by twice. These simulations thus show that demanding cyclic tests can be adequately represented by the comparatively simple fabric model. The quality of the deformation prediction is still insufficient, which is why a further material model should be used for the simulation of cyclic processes for control purposes.

The simulations with ISA model are shown in Fig. 8d-f and 9d-f for initial relative densities of $D_{r0} = 44\%$ and 72%, respectively. With this material model it is possible to consider different soil fabric in situ via the fabric factor r_F. This parameter has a significant influence on the course of $q(\varepsilon_1)$ and $\varepsilon_v(\varepsilon_1)$, whereby smaller values of r_F provide a more dilatant behavior at the same void ratio e, as observed for moist tamped samples compared to samples prepared by dry air pluviation. (Fuentes 2014) therefore proposed $r_F = 1.6$ for tests on dry air pluviated samples and $r_F = 0$ for tests on samples prepared by moist tamping. As described in Sec. 3 the specimens of the tests considered here were prepared by means of dry air pluviation. For a structure factor $r_F = 1.5$, see Tab. 2, a very good agreement of the accumulated volumetric strains between the simulation and the test can be observed for both samples. This optimal r_F value derived from the simulations agrees well with the structure factor $r_F = 1.6$ proposed by Fuentes for this type of sample preparation. In general, a partially better simulation result than with HYpo+IGS is observed. However, the transition from the elastic to the plastic region is visible based on the kink in the $\tau/p\text{-}\gamma$ hysteresis, which can be explained by the elastoplastic formulation of the intergranular strain of the model. In contrast, this kink is not evident in triaxial tests with the ISA model (Duque et al. 2022, Fuentes, Tafili and Triantafyllidis 2018, Machacek et al. 2021, Tafili 2019, Tafili and Triantafyllidis 2020, Tafili et al. 2022). As soon as the intergranular strain yield surface is exceeded, the model describes a hypoplastic behavior. The accumulated volumetric strain ε_v is slightly overestimated for the medium dense specimen, which follows from an underestimation of the dilatancy. However, given the more accurate description of the material behavior with the ISA model compared to Hypo+IGS, five more material parameters are needed for ISA as well (compare Tab. 1 with Tab. 2).

Figs. 8g-i and 9g-i show the simulations with the Sanisand model. A significant parameter in the Sanisand model is the material constant n_d, which describes the inclination of the dilatancy surface in the $p\text{-}q$-plane. For high values of n_d, dilatancy is predicted to occur well before the critical state line CSL is reached, which can lead to an underestimation of the accumulated positive volumetric strain ε_v. Small values of n_d, on the other hand, almost completely eliminate dilatancy, leading to an overestimation of the accumulated positive volumetric strain ε_v. The correct calibration and choice of the material constant n_d is therefore essential to describe dilatancy effects accurately in simulations with the Sanisand model. The present simulations show that the hysteresis loops can be well reproduced with the Sanisand model for $n_d = 1.5$ for both the medium dense and dense samples. Especially, the numerical calculations for the dense sample are very close to the experimental results.
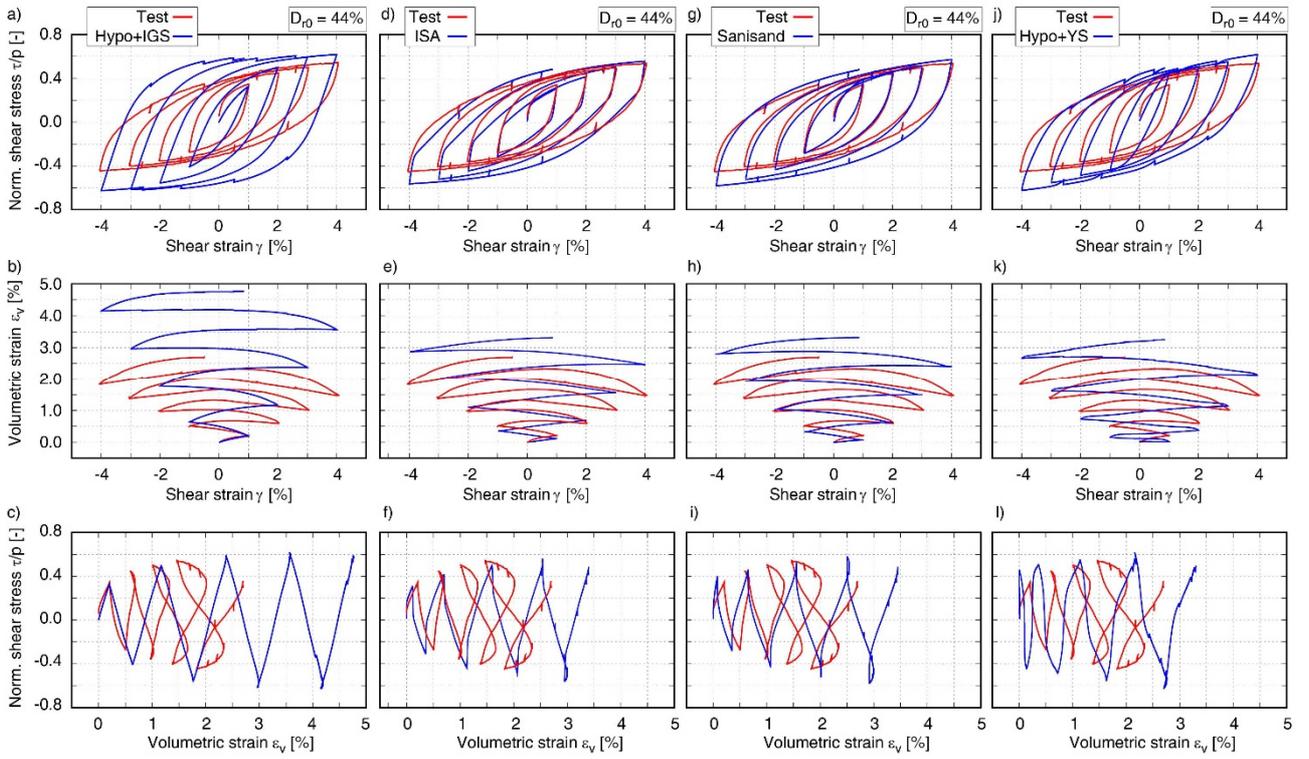
Figure 8. Test (red) and simulations (blue) for the medium dense sample ($D_{r0} = 44\%$): a-c) Hypo+IGS, d-f) ISA, g-i) Sanisand and j-l) Hypo+YS
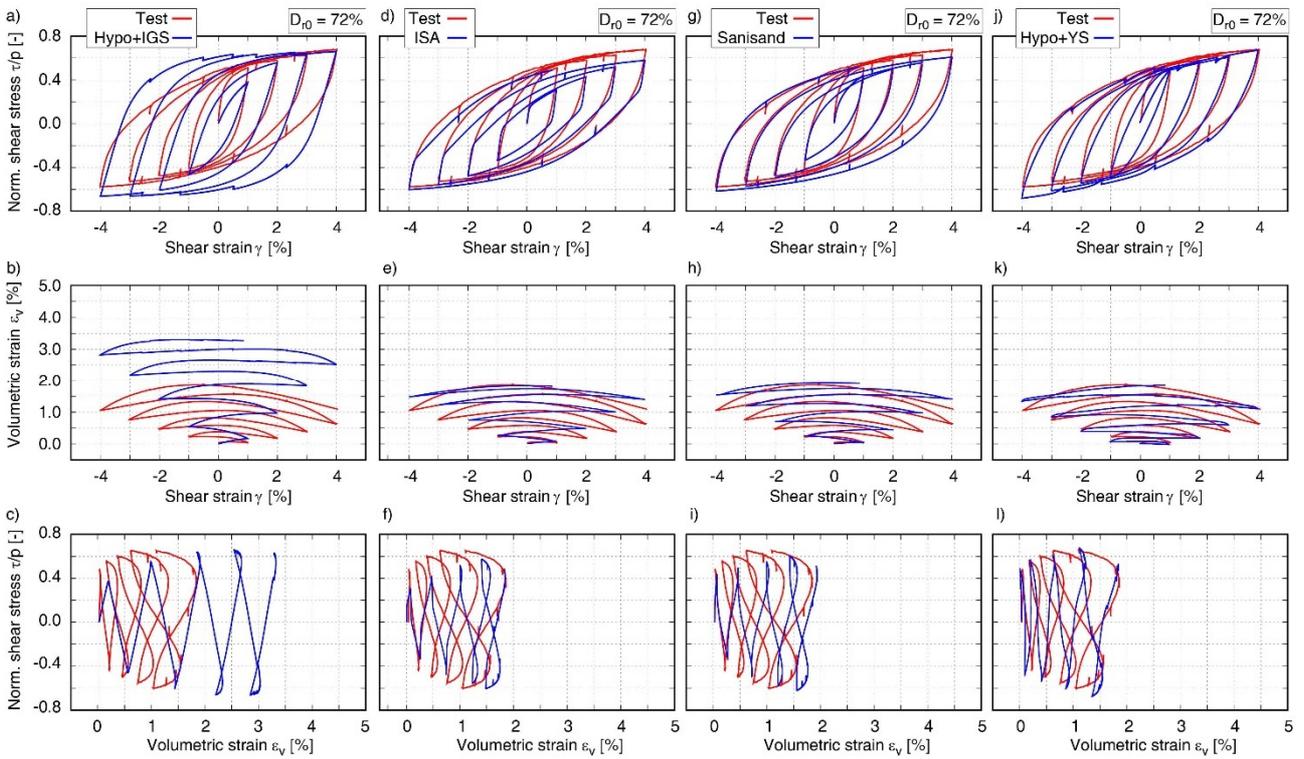
Figure 9. Test (red) and simulations (blue) for the medium dense sample ($D_{r0} = 72\%$): a-c) Hypo+IGS, d-f) ISA, g-i) Sanisand and j-l) Hypo+YS

Furthermore, it can be seen that the Sanisand model describes a smoother transition from elastic to plastic behavior than the ISA model. The good description of the Sanisand model is enabled by the parameter m which characterizes the elasto-plastic transition. Here, m controls the transition range from low stresses to stresses in the region of the limiting compression curve LCC.

The simulations with the newly proposed model with historiotropic surface are depicted in Figs. 8j-l and 9j-l for initial relative densities of $D_{r0} = 44\%$ and 72%, respectively. It can be observed that the experimental results for both the medium dense and dense specimens are well simulated with the same set of parameters. The model introduces the so-called overconsolidation ratio OCR with power $-n_0$ (resulting in a material parameter), which can be used to distinguish between initial loading and unloading and reloading. Choosing a higher value of n_0 would result in a lower dilatancy, thus increasing accumulated volumetric strain.

The phase transformation line PTL depends on the stress and void ratio, its slope is described in Hypo+IGS by the friction angle φ_{PTL}. Dense sands reach PTL at lower stress ratios η_{PTL} than loose sands. When the parameter $n_{\mathrm{PTL}} = 1.0$ and the ratio of the actual void ratio to the critical void ratio reaches $e/e_c = 1$, the friction angle φ_{PTL} corresponds exactly to the critical friction angle φ_c in this model. If a larger value of φ_{PTL} is chosen, the PTL in the stress space will lie below the CSL. This would lead to an overestimation of the dilatancy and thus an underestimation of the accumulated volumetric strain under cyclic loading if the parameter φ_{PTL} is not chosen properly. Here, a combination of $n_0 = 1.2$ and $n_{\mathrm{PTL}} = 2$ resulted in best agreement between model prediction and laboratory test for both experiments.

In summary, it can be concluded that the material behavior observed in the torsional cyclic tests from the hollow cylinder apparatus is most accurately described by Sanisand and the hypoplastic material model with historiotropic yield surface (Hypo+YS).

7. Conclusion and outlook

Cyclic triaxial tests on hollow cylinder samples of fine sand have been performed. Samples with two different desities were prepared by air pluviation and tested under fully saturation. On each sample the cycles were applied by torsional angles for shear strains $\gamma = 1$, 2, 3 and 4%. Shear wave velocity measurements with bender elements, were taken to derive the degradation of the shear modulus G.

Four constitutive models have been used to model numericaly the torsional shear tests conducted in the hollow cylinder apparatus. All models showed satisfactory agreement with laboratory data, whereby hypoplasticity with intergranular strain overestimates the shear stress as well as the evolution of the volumetric strain, especially for the medium dense sample. The ISA model shows a kink in the shear stress - shear strain $(\tau/p\text{-}\gamma)$ hysteresis when reaching the elastic intergranular yield surface, while the Sanisand model as well as the recently proposed hypoplastic material model with historiotropic yield surface best represent the mechanical behavior of the material in these tests over the entire range.

References

Baziar, M.H., and H. Sharafi. 2011. "Assessment of silty sand liquefaction potential using hollow torsional tests – An energy approach." *Soil Dynamics and Earthquake Engineering*, vol. 31, pp. 857-865.

Been, K., and M. G. Jefferies. 1985. "A state parameter for sands". *Géotechnique*, vol. 35, no.2, pp. 99-112.

Bishop, A.W. and A.K.G. Eldin. 1953. "The effect of stress history on the relation between ϕ and the porosity in sand." In *Proc. 3rd Int. Conf. Soil Mech. & Found. Eng.*, Switzerland, vol. 1, pp. 100-105.

Bolton, M.D. 1986. "The strength and dilatancy of sands." *Géotechnique*, vol. 36, no. 1, pp. 65-78.

Chakraborty, T., and R. Salgado. 2010. "Dilatancy and shear strength of sand at low confining pressures." *Journal of Geotechnical and Geoenvironmental Engineering, ASCE*, vol. 136, no. 3, pp. 527-532.

Dafalias, Y. F., and M. Manzari. 2004. "Simple plasticity sand model accounting for fabric change effects." *Journal of Engineering Mechanics*, vol. 130, no. 6, pp. 622-634.

Y. F. Dafalias and M. Taiebat. 2016. "Sanisand-z: zero elastic range sand plasticity model." *Géotechnique*, vol. 66, no. 12, pp. 999-1013.

De Silva, L., J. Koseki, S. Wahyudi, and Sato, T. 2014. "Stress-dilatancy relationships of sand in the simulation of volumetric behavior during cyclic torsional shear loadings." *Soils and Foundations*, vol. 54, no. 4, pp. 845-858.

Duque, J. M. Tafili, G. Seidalinov, D. Mašín, and W. Fuentes. 2022. "Inspection of four advanced constitutive models for fine-grained soils under monotonic and cyclic loading." *Acta Geotechnica*. DOI: 10.1007/s11440-021-01437-w

Frossard, E. 1979. "Effects of sand grain shape on interpar-ticle friction; indirect measurements by Rowe's stress dilatancy theory." *Géotechnique*, vol. 29, no. 3, pp. 341-350.

Fuentes, W., M. Tafili, and T. Triantafyllidis. 2018. "An ISA-plasticity-based model for viscous and non-viscous clays." *Acta Geotechnica*, vol. 13, no. 3, pp. 367-386.

Fuentes, W., and Th. Triantafyllidis. 2015. ISA model: A constitutive model for soils with yield surface in the intergranular strain space. *International Journal for Numerical and Analytical Methods in Geomechanics*, vol. 39, no. 11, pp. 1235-1254.

Fuentes Lacouture, W.M. 2014. "Contributions in Mechani-cal Modelling of Fill Materials." Dissertation, Institute for Soil Mechanics and Rock Mechanics, Karlsruhe Institute of Technology (KIT), no. 179.

Georgiannou, V.N., and A. Tsomokos. 2008. "Comparison of two fine sands under torsional loading." *Canadian Geotechnical Journal*, vol. 45, pp. 1659-1672.

C.E. Grandas Tavera, Th. Triantafyllidis, and L. Knittel. 2020. "A constitutive model with a historiotropic yield surface for sands." In *Recent Developments of Soil Mechanics and Geotechnics in Theory and Practice*, pp. 13-43, editor Th. Triantafyllidis, Springer.

Guo, P., and X. Su. 2007. "Shear strength, interparticle locking, and dilatancy of granular materials." *Canadian Geotechnical Journal*, vol. 44, no. 5, pp. 579-591.

Houlsby, G.T. 1991. "How the dilatancy of soils affects their behaviour." Technical Report 121/91, University of Oxford, Department of Engineering Science.

Jacobsen, H.M. 1989. "Dilatancy and cohesion in frictional materials." XII ICFMFE, Rio de Janeiro.

Kabilamany, K. and K. Ishihara. 1990. "Stress dilatancy and hardening laws for rigid granular model of sand." *Soil Dynamics and Earthquake Engineering*, vol. 9, no. 2, pp. 66-77.

Knittel, L. 2020. "Granular soils under multidimensional cyclic loading." Dissertation, Institute for Soil Mechanics and Rock Mechanics, Karlsruhe Institute of Technology (KIT), no. 188, 2020.

Lashkari, A. 2010. A SANISAND model with anisotropic elasticity. *Soil Dynamics and Earthquake Engineering*, vol. 30, no. 12, pp. 1462-1477.

Li, X.S. 2002. "A sand model with state-dependent dilatancy." *Géotechnique*, vol. 52, no. 3, pp. 173-186.

Li, X.S. and Y.F. Dafalias. 2000. "Dilatancy for cohesionless soils." *Géotechnique*, vol. 50, no. 4, pp. 449-460.

Li, X.S. Y.F. Dafalias, and Z.L. Wang. 1999. "Statedependent dilatancy in critical-state constitutive modelling of sand." *Canadian Geotechnical Journal*, vol. 36, no. 4, pp.599-611.

Liu, H. Y. and F. Pisanò. 2019. "Prediction of oedometer terminal densities through a memory-enhanced cyclic model for sand." *Géotechnique Letters*, vol. 9, no. 2, pp. 81-88.

Liu, H. A. Diambra, J.A. Abell, and F. Pisanò, 2020. "Memory-Enhanced Plasticity Modeling of Sand Behavior under Undrained Cyclic Loading." *Journal of Geotechnical and Geoenvironmental Engineering*, vol. 146, no. 11.

Luong, M.P. 1982. "Mechanical aspects and thermal effects of cohesionless soils under cyclic and transient loading." In *Proc. IUTAM Conf. on Deformation and Failure of Granular materials*, Delft, pp. 239-246.

Machaček, J., P. Staubach, M. Tafili, H. Zachert and T. Wichtmann. 2021. Investigation of three sophisticated constitutive soil models: From numerical formulations to element tests and the analysis of vibratory pile driving tests. *Computers and Geotechnics*, vol. 138, no. 10.

Niemunis, A. 2022. Download Package of Incremental Driver. https://soilmodels.com. Last access: 20.09.2022.

Niemunis, A. 2003. "Extended hypoplastic models for soils." Habilitation. Veröffentlichungen des Institutes für Grundbau und Bodenmechanik, Ruhr-Universität Bochum, Heft Nr. 34.

Niemunis A., and I. Herle. 1997. "Hypoplastic model for cohesionless soils with elastic strain range." *Mechanics of Cohesive-Frictional Materials*, vol. 2, pp. 279-299.

Niemunis, A., and L. Knittel. 2020. Removal of the membrane penetration error from triaxial data. Open Geomechanics, vol. 2, no. 5. DOI: 10.5802/ogeo.7

Poblete, M., W. Fuentes, and Th. Triantafyllidis. 2016. "On the simulation of multidimensional cyclic loading with intergranular strain." *Acta Geotechnica*, vol. 11, pp. 1263-1285.

Pradhan T.B.S., and F Tatsuoka. 1989. "On stress-dilatancy equations of sand subjected to cyclic loading." *Soils and Foundations*, vol. 29, no. 1, pp. 65–81.

Pradhan, T.B.S., F. Tatsuoka, and Y. Sato. 1989. "Experimental stress-dilatancy relations of sand subjected to cyclic loading." *Soils and Foundations*, vol. 29, no. 1, pp. 45-64.

Roscoe, K.H. 1970. "The influence of strains in soil mechanics." *Géotechnique*, vol. 20, no. 2, pp. 129-170.

Rowe, P.W. 1962. "The stress-dilatancy relation for static equilibrium of an assembly of particles in contact." *Proceedings of the Royal Society London*, Ser. A, vol. 269, pp. 500-527.

Schanz, T. , and P.A. Vermeer 1996. "Angles of friction and dilatancy of sand." *Géotechnique*, vol. 46, no. 1, pp. 145-151.

Shahnazari, H., and I. Towhata. 2002. "Torsion shear tests on cyclic stress-dilatancy relationship of sand." *Soils and Foundations*, vol. 42, no. 1, pp. 105-119.

Simo, J. and T. Hughes. 1998. "Computational inelasticity." Springer, New York.

Tafili, M. 2020. "On the Behaviour of Cohesive Soils: Constitutive Description and Experimental Observations. PhD thesis, Institute of Soil Mechanics and Rock Mechanics, Karlsruhe Institute of Technology.

Tafili, M., G. Medicus, M. Bode, and W. Fellin. 2022. Comparison of two small-strain concepts: Isa and intergranular strain applied to barodesy. *Acta Geotechnica*. DOI: 10.1007/s11440-022-01454-3

Tafili, M., and T. Triantafyllidis. 2020. AVISA: anisotropic visco-ISA model and its performance at cyclic loading. *Acta Geotechnica*, vol. 15, pp. 2395-2413.

Taiebat, M., and Y. F. Dafalias. 2007. "SaniSand: Simple anisotropic sand plasticity model." *International Journal for numerical and analytical methods in geomechanics*, vol. 32, no. 8, pp. 915-946.

Tatsuoka, F. 1976. "Stress-dilatancy relations of anisotropic sands in three dimensional stress condition." *Soils and Foundations*, vol. 16, no. 2, pp. 1-18.

Tatsuoka, F. 1987. "Discussion of "The strength and dilatancy of sands" by M.D. Bolton." *Géotechnique*, vol. 7, no. 2, pp. 219- 225.

Tatsuoka, F., K. Ochi, S. Fujii, and M. Okamoto. 1986. "Cyclic undrained triaxial and torsional shear strength of sands for different sample preparation methods." *Soils and Foundations*, vol. 26, no. 3, pp. 23-41.

Taylor, D.W. 1948. "Fundamentals of soil mechanics." Wiley, New York.

Tokue, T. 1979. "Deformation behaviours of dry sand under cyclic loading and a stress-dilatancy model." *Soils and Foundations*, vol. 19, no. 2, pp. 63-78.

Vaid, Y.P. and S. Sasitharan. 1992. "The strength and dilatancy of sand." *Canadian Geotechnical Journal*, vol. 29, pp. 522-526.

Wolffersdorff, P.-A. von. 1996 "A hypoplastic relation for granular materials with a predefined limit state surface." Mechanics of Cohesive-Frictional Materials, vol. 1, pp. 251-271.

Wan, R.G. and P.J. Guo. 1999. "A pressure and density dependent dilatancy model for granular materials." *Soils and Foundations*, vol. 39, no. 6, pp. 1-11.

Wan, R.G. and P.J. Guo. 2004. "Stress dilatancy and fabric dependencies on sand behavior." *Journal of Engineering Mechanics*, vol. 130, no. 6, pp. 635-645.

Wichtmann, T., W. Fuentes, and T. Triantafyllidis. 2019. Inspection of three sophisticated constitutive models based on monotonic and cyclic tests on fine sand: Hypoplasticity vs. Sanisand vs. ISA. *Soil Dynamics and Earthquake Engineering*, vol. 124, pp. 172-183.

Yamashita, S. and S. Toki. 1993. Effects of fabric anisotropy of sand on cyclic undrained triaxial and torsional strengths. Soils and Foundations, vol. 33, no. 3, vol. 92-104.

Yoshimine, M., K. Ishihara, and W. Vargas. 1998. "Effects of principle stress direction and intermediate principal stress on undrained shear behavior of sand." *Soils and Foundations*, vol. 38, no. 3, pp. 179-188.